Frequency and Time Domain Characterization of Microstrip-Ridge Structures

Andrew G. Engel, Jr. and Linda P. B. Katehi, *Senior Member, IEEE*

Abstract— Microstrip-ridge structures, i.e., conducting strips which are mounted on ridges and are in the close proximity of other conductors on other ridges, are found in sub-millimeter/terahertz monolithic circuits in conjunction with layered, ridged dielectric waveguides; in millimeter-wave monolithic circuits as microslab lines; in microwave monolithic circuits as integrated traveling-wave optical modulators; and in VLSI circuits as interconnects. A hybrid full-wave frequency domain technique which uniquely synthesizes well-known integral equation and mode-matching methods is shown to be applicable to the study of microstrip-ridge structures. Unlike most other integral equation techniques, the integral equation–mode matching (IEMM) technique is capable of characterizing a wide variety of *nonplanar* structures. Time domain results are obtained by utilizing a Fourier transform and an equivalent circuit model to evaluate the response at each frequency point. To introduce this method, several two-dimensional structures—specifically, coupled microstrips on ridges, coupled microstrip with an etched groove, and an electrooptic modulator—are examined.

I. INTRODUCTION

As monolithic circuits are designed to perform multiple functions at heightened frequencies, increased complexity is inevitable. One reason why monolithic circuits are becoming more elaborate is the use of a class of nonplanar interconnects, which may be described as "microstrip-ridge structures." These structures are microstrip in that they consist of conducting strips suspended by a dielectric above a ground plane, but the conducting strips are mounted on ridges and in the close proximity of other conductors on other ridges. For example, in the sub-millimeter and terahertz frequency ranges, excessive ohmic losses preclude the use of microstrip in monolithic circuits. Whether coplanar waveguide, dielectric waveguide, or another type of guiding structure is used in place of microstrip, sub-millimeter/terahertz monolithic circuits apparently will still employ short lengths of microstrip-ridge structures. A typical sub-millimeter/terahertz monolithic circuit could utilize a low-loss layered, ridged dielectric waveguide as a transmission line [1]. A passive circuit element such as an inductor could be created from the selective use of conductors in conjunction with the waveguide. A transition to
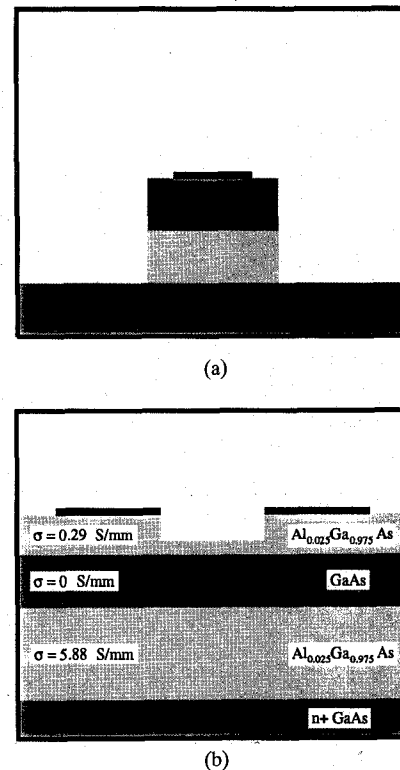
(a)

(b)

Fig. 1. Examples of microstrip-ridge structures include cross sections of (a) a conducting strip on layered ridged dielectric waveguide, and (b) an electrooptic modulator.

an active device could consist of a conductor mounted on the ridged waveguide (Fig. 1(a)). A millimeter wave monolithic circuit might employ a microslab™ waveguide [2], [3], which consists of a conducting strip on a ridge with a layered substrate. Microwave signals are used to control the permittivity of optical waveguides, as in an integrated traveling-wave optical modulator. The modulator structure might have an etched groove between two conductors (Fig. 1(b)) in order to improve the modulator bandwidth. Microwave harmonics associated with very narrow pulses are also carried by complicated interconnects in VLSI applications. These interconnects, which are designed with the intention of increasing packing density without increasing crosstalk, might consist of noncoplanar conductors fabricated in conjunction with dielectric ridges, grooved substrates, and localized superstrates. The dispersion of the microwave signals could have significant effects on pulse propagation.

Over the past ten years, the characterization of microstrip structures on and near dielectric ridges has been addressed

several times. Quasi-static methods, such as an integral equation formulation [4] and the rectangular boundary division method [5], [6], have considered an open microstrip on a finite dielectric and shielded microstrip near a chip edge, respectively. In addition, full-wave mode-matching techniques have been applied to the analysis of microslab [2], [3], transverse wave propagation on FET structures [7], and a variety of quasi-planar structures involving conductors on finite-width substrates [8]. The method of lines [9], [10] has been employed to characterize electrooptic modulator structures, a microstrip on a ridged substrate, a microstrip near a chip edge, microslab, and slow-wave MIS microstrip/coplanar lines with inhomogeneously doped substrates. In addition, finite element [11], finite difference [12], [13], transmission-line matrix (TLM) [14], and boundary integral [15] techniques may be applied to structures with conducting strips in the presence of inhomogeneous dielectrics.

Although nonplanar strip-ridge structures have not been typically characterized by the class of integral equation/method of moments techniques which solve directly for the currents on the conducting strips, nonplanar analysis based on these techniques is possible. In this paper, a hybrid full-wave integral equation–mode matching (IEMM) technique is described and applied to the study of nonplanar strip-ridge structures in both the frequency and time domains. The IEMM technique analytically decouples a structure into two parts, namely, the conducting strips and the supporting dielectrics. The integral equation portion of the formulation solves the conductor problem, and the mode matching portion solves the dielectric problem.

As is demonstrated in other works (e.g., [16]), the strength of the IEMM method lies in its ability to characterize a class of three-dimensional structures in which the uniformity of the dielectric support structure along the longitudinal direction is preserved. When these structures are analyzed, the decoupling of the dielectric problem from the conductor problem by the IEMM method is exploited—the mode matching portion of the technique is applied to a given dielectric support structure independent of the placement of conducting strips, and efficient and swift solution of the integral equation with the method of moments is then possible for any configuration of conductors on the dielectric support structure. The extension to three dimensions is easily accomplished by changing the dependence of the longitudinal coordinate from an exponential function (i.e., a propagating wave) to a sine or cosine function (i.e., a standing wave). The IEMM method requires that only the conducting strips be discretized, and this area is usually a small portion of the structure which is characterized; in contrast, many of the other techniques need to discretize the entire volume of the structure or all of the interfaces between dielectrics for 3D implementation.

The 2D IEMM technique was briefly described for a specific class of structures in [17]. The objectives of this paper are to give a more general description of the 2D method and to present frequency and time domain studies of several 2D structures—specifically, coupled microstrip on ridges, coupled microstrip with an etched groove, and an electrooptic modulator.
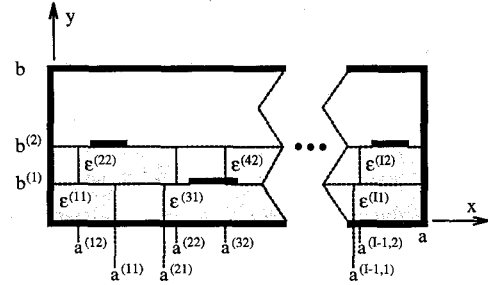

Fig. 2. Geometry of the general structure.

II. THEORY

The IEMM technique is applied by modeling a structure as a rectangularwaveguide with conducting strips supported by dielectric layers which contain rectangular step-inhomogeneities (Fig. 2). The waveguide is divided into adjacent sections of layered parallel-plate waveguide. The Green's function is determined by replacing the conducting strips with a delta-function excitation and employing mode matching to apply the boundary conditions at the interfaces between the parallel-plate waveguides. The boundary conditions on the conducting strips are enforced by solving the electric field integral equation with the method of moments. Useful quantities such as the propagation constant, the characteristic impedance, and a coupling coefficient may then be calculated, and a time domain analysis technique may be employed to characterize pulse propagation.

A. General Structure

The general structure contains rectangular step inhomogeneities and conductingstrips, as shown in Fig. 2. The structure is uniform in the z-direction. The outer walls are perfect electric conductors. Along the y-axis, the structure is divided into J sections at $y = b^{(j)}, j = 1, 2, \cdots, J-1$. (For simplicity, Fig. 2 is drawn with only three sections.) The width of the jth section is $d^{(j)} = b^{(j)} - b^{(j-1)}$. The jth section is divided into I layers along the x-axis at $x = a^{(ij)}, i = 1, 2, \cdots, I - 1$. The value of I varies depending on the section index j. Each layer is isotropic with permittivity $\epsilon^{(ij)}$ and permeability $\mu^{(ij)}$. Dielectric losses are accounted for with complex values of permittivity. The structure contains a total of M conducting strips, and the y-dimensions of the strips are assumed to be negligible. This paper only considers strips which are located parallel to the x-axis.

B. Integral Equation and Green's Function

The fields, currents, and propagation constants of the structure are determined by solving Pocklington's integral equation in the spatial domain. For a two-dimensional structure such as the one under consideration, the integral equation reduces to

$$\overline{E} = \int_{S'} \overline{\overline{G}}_E \cdot \overline{J} \, dS' \tag{1}$$

where $\overline{\overline{G}}_E$ is the dyadic electric field Green's function associated with the structure, $\overline{J}$ is the current in the conducting

strips, and S' represents the surfaces of the conducting strips. The Green's function is the electric field when the conducting strips are replaced with a current line source at (x', y').

A convenient form of the Green's function is derived by considering eachsection of the structure as a section of inhomogeneous parallel plate waveguide [1]. In each section, the fields consist of infinite sums of TE_x and TM_x modes. The fields away from the source obey the homogeneous wave equation, and are determined using vector potentials $\overline{A} = a_x(x, y, z)\hat{x}$ and $\overline{F} = f_x(x, y, z)\hat{x}$ via

$$\overline{E} = -j\omega\overline{A} + \frac{1}{j\omega\epsilon\mu}\nabla\nabla\cdot\overline{A} + \frac{1}{\epsilon}\nabla\times\overline{F} \qquad (2)$$

$$\overline{H} = \frac{1}{\mu}\nabla\times\overline{A} + j\omega\overline{F} - \frac{1}{j\omega\epsilon\mu}\nabla\nabla\cdot\overline{F} \qquad (3)$$

where a time convention of $e^{j\omega t}$ has been chosen.

Since the structure is rectangular, the x-, y-, and z-dependencies of a_x and f_x are separable. Assuming the z-dependence to be $\exp(-jk_z z)$, a_x and f_x in each layer are expressed as

$$f_x^{(ij)}(x, y, z) = \sum_l X_l^{(ij)E}(x) Y_l^{(j)E}(y) \exp(-jk_z z) \qquad (4)$$

$$a_x^{(ij)}(x, y, z) = \sum_l X_l^{(ij)M}(x) Y_l^{(j)M}(y) \exp(-jk_z z) \qquad (5)$$

where the superscripts i and j indicate the layer and section and the superscripts E and M refer to TE_x and TM_x modes, respectively. The separation parameters associated with the functions $X_l^{(ij)}, Y_l^{(j)}$ and $\exp(-jk_z z)$ are $k_{xl}^{(ij)}, k_{yl}^{(j)}$, and k_z, respectively. The separation parameters and the wavenumber of each layer $k^{(ij)} = \omega\sqrt{\epsilon^{(ij)}\mu^{(ij)}}$ are related by the dispersion equation.

The boundary conditions at each layer interface and at the conducting walls at $x = 0, a$ are used to generate transcendental equations for the x-directed wavenumbers $k_{xl}^{(ij)}$ and expressions for the unknown constants associated with the x-dependence $X_l^{(ij)}$ [18].

The y-dependencies of the fields consist of infinite sums ofplane waves. For convenience in the application of the boundary conditions, the y-dependence of the fields in the section which contains the current source is separated into two parts, which are designated the primary and secondary fields. The primary fields exist only in the section which contains the source, satisfy the boundary conditions at the source, and consist of plane waves leaving the source in the $\pm y$ -direction. Expressions for the primary field y-dependence $Y_{Pl}^{\lessgtr(j)}(y, y')$ and mode amplitudes $C_{Pl}^{<(j)}$ and $C_{Pl}^{>(j)}$ are explicitly determined by the boundary conditions at the source $(y = y')$ and are given in Appendix I. The secondary fields satisfy the homogeneous wave equation in all regions and consist of plane waves traveling in both directions with mode amplitudes $C_l^{(j)}$ and $D_l^{(j)}$. The secondary field mode amplitudes are determined by enforcing the boundary conditions at each section interface with mode matching (extending the work

in [1] by applying [19]–[22]) and combining the resulting scattering matrix equations.

In order to relate the fields in all sections, reflection coefficient matrices are defined for waves at the interfaces between sections. At the interface $y = b^{(j-1)}$, in the jth section, when $y < y'$, and when section j does not contain the source (so that the primary fields are zero), the reflection coefficient matrix $\Gamma^{<(j)}$ relates the secondary field mode amplitudes by

$$C^{(j)} = \Gamma^{<(j)} D^{(j)} \qquad (6)$$

where $C^{(j)}$ and $D^{(j)}$ are vectors which contain the mode amplitudes and have the general form given in (25), Appendix II. Equation (6) and the definition of the interface scattering matrix in Appendix II are combined to give

$$\Gamma^{<(j+1)} = S_{22}^{(j)} + S_{21}^{(j)}$$
$$\cdot (-S_{11}^{(j)} + (L^{(j)-1}\Gamma^{<(j)}L^{(j)-1})^{-1})^{-1} S_{12}^{(j)} \qquad (7)$$

where

$$L^{(j)\pm 1} = \text{diag}\{\exp(\pm jk_{yl}^{(j)} d^{(j)})\} \qquad (8)$$

and $S_{mn}^{(j)}$ are the elements of the interface scattering matrix. Similarly, at the interface $y = b^{(j)}$, in the jth section, when $y > y'$, and when section j does not contain the source, the reflection coefficient matrix $\Gamma^{>(j)}$ relates the secondary field mode amplitudes by

$$D^{(j)} = \Gamma^{>(j)} C^{(j)} \qquad (9)$$

so that

$$\Gamma^{>(j)} = S_{22}^{(j)} + S_{21}^{(j)}(-S_{11}^{(j)}$$
$$+ (L^{(j+1)-1}\Gamma^{>(j+1)}L^{(j+1)-1})^{-1})^{-1} S_{12}^{(j)}. \qquad (10)$$

Since the ends of the waveguide at $y = 0$ and $y = b$ are perfectly conducting walls, $\Gamma^{<(1)} = \Gamma^{>(J)} = -I$. Repeated use of (7) and (10) gives $\Gamma^{<(j)}$ and $\Gamma^{>(j)}$ for the section which contains the source.

When the reflection coefficient equations are applied at the boundaries of thesection which contains the source, the primary fields must be taken into account. As shown in Appendix II, once the primary fields have been included, the secondary field mode amplitudes $C_l^{(j)}$ and $D_l^{(j)}$ in the source section are known in terms of the primary field mode amplitudes $C_{Pl}^{\lessgtr(j)}$.

The electric field Green's function is expressed as

$$G_{Ezz}^{(j)}(x, y; x', y') = [U_1^{(j)}(x, y)]^T R^{(j)} U_2^{(j)}(x', y') \qquad (11)$$

where $R^{(j)}$ is a matrix which depends on whether $y' < y$ or $y' > y$, the index j is determined by which section contains y', and $U_1^{(j)}$ and $U_2^{(j)}$ are vectors which contain the explicit dependence of the Green's function on (x, y) and (x', y'), respectively. Expressions for $R^{(j)}, U_1^{(j)}$, and $U_2^{(j)}$ are given in Appendix II. The matrix $R^{(j)}$ contains information about the dielectric support structure relative to section j. When three-dimensional structures are evaluated, $R^{(j)}$ may be determined for each section of a given dielectric support structure, and

efficient and swift analysis is possible for any configuration of conductors which are placed parallel to the x- or y-axis on the dielectric support structure. No such advantage is present in the two-dimensional case since the propagation constant β is determined iteratively and $R^{(j)}$ must be recalculated for each value of β.

C. Method of Moments Solution

The method of moments is applied by expressing the currents on the conductors in terms of basis functions $\Psi_m(x)$ with unknown coefficients I_m. Since all of the structures which are characterized in the next section have conductors which are narrow compared to guided wavelength, the current on each conductor is assumed to have a negligible transverse component and is modeled with a Maxwellian function [23].

The boundary conditions on the conducting strips are applied with Galerkin's technique, and the resulting matrix equation is

$$[V] = [Z][I] \tag{12}$$

where $[V]$ is the excitation vector, $[I]$ is the vector of unknown current coefficients, and $[Z]$ is the $M \times M$ impedance matrix with elements given by

$$
\begin{aligned}
Z_{m'm} = \int_{x_{m'}-W_{m'}/2}^{x_{m'}+W_{m'}/2} \int_{x_m-W_m/2}^{x_m+W_m/2} \\
\cdot\, G_{Ezz}(x, y = y_{m'}; x', y' = y_m) \\
\cdot\, \Psi_m(x')\, \Psi_{m'}(x)\, dx'\, dx.
\end{aligned}
\tag{13}
$$

The left-hand side of (12) is zero since E_z vanishes on the conducting strips, and the propagation constants for the structure are determined from zeros of the determinant of $[Z]$ since (12) is a homogeneous system. In general, the propagation constant $\gamma = jk_z$ may be complex, and is expressed in terms of the phase constant β and the attenuation constant α as $\gamma = \alpha + j\beta$. Once the propagation constant is known, the fields for a given mode can be calculated from the integral equation.

D. Characteristic Impedance, Coupling Coefficient, and Time Domain Analysis

The characteristic impedance Z_c of a given mode in a structure is determined from a reciprocity-related characteristic impedance definition [24], [25], which is chosen because it converts the modal description of general, asymmetric multiconductor lines into a form where the equivalent voltages and currents are compatible with external device models.

In the case where coupled lines are evaluated, the coupling is quantified with the coupling coefficient k_c, given by [26], as the square root of the ratio of the coupled power to the incident power. The expression for k_c is given in Appendix III.

Pulse propagation in the time domain on the structures is characterized by transforming the excitation to the frequency domain, utilizing an equivalent circuit model [27] to evaluate the response at each frequency point, and transforming back to the time domain. The equivalent circuit model considers the modes of a system of terminated transmission lines as
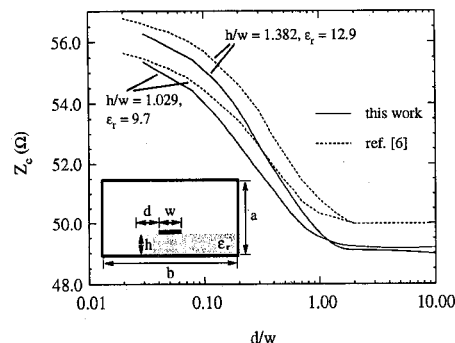

Fig. 3. Comparison of characteristic impedance results from this work to results from [6]. The center of the strip is aligned with $b/2$, $w = 1.0$ mm, $a = b = 27.6$ mm, and frequency = 3 GHz.
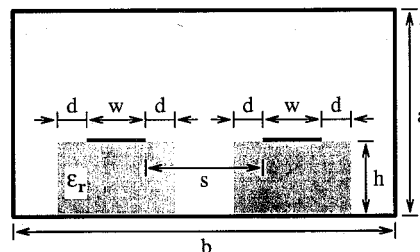

Fig. 4. Geometry of two coupled microstrips on dielectric ridges: $w = 0.1$ mm, $h = 0.1$ mm, $d = 0.05$ mm, $a = 1.3$ mm, $b = 2.51$ mm, and $\epsilon_r = 12.85$.
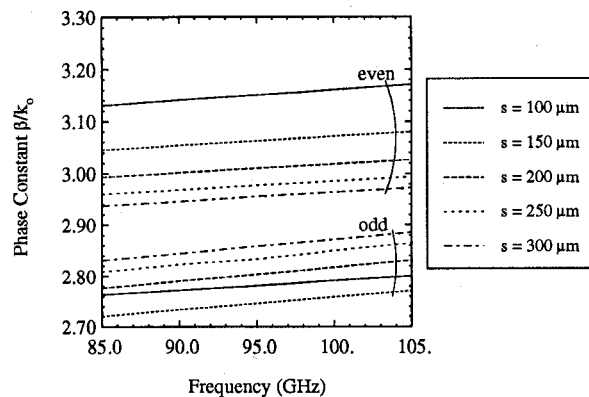

Fig. 5. Phase constant β versus frequency at various spacings s for the structure described in Fig. 4.

equivalent decoupled lines of unit characteristic impedance. The spatial variation of the equivalent voltages and currents for a given mode is described by the propagation constant, which is calculated from the IEMM analysis, and by two coefficients, which are calculated from the boundary conditions at the terminations. The equivalent quantities are related to the physical quantities through coupling matrices which depend upon the modal coefficients of the physical currents and the characteristic impedance of each mode.

III. RESULTS

The software was developed on an HP/Apollo workstation, and the calculations were performed on HP/Apollo, HP 9000, and IBM RS-6000 computers. In all cases presented here, the

propagation constant values were well converged using 100 TE_x and 100 TM_x modes in each section. The characteristic impedance calculations required 140 TE_x and 140 TM_x modes in each section. As with all hybrid techniques, the efficiency of the IEMM method is highly dependent on the geometry of the problem being solved. The CPU time required by the integral equation portion of the code depends on the conductor geometry, and the time required by the mode matching depends on the dielectric geometry. Specifically, for the propagation constant calculations, an HP 9000/720 workstation needs 2 CPU min for each mode matching interface and 5 min to calculate the Green's function matrix $R^{(j)}$ and solve the integral equation. Propagation constants are typically determined in fewer than ten iterations. These CPU times reflect the current state of the code, and do not reflect any fundamental limit on the efficiency of the method. Techniques are available which could greatly reduce the computation times.

A. Verification

The software has been extensively verified. Results for simple microstrip and coupled microstrip were compared with the multitudinous data available in the literature; excellent agreement was obtained. The propagation constant as a function of frequency for a microstrip near a chip edge was calculated using the IEMM method, and was shown to agree well with results obtained from both the method of lines and experiment [17]. Results for the characteristic impedance for a similar structure on two substrates of differing permittivities and heights are compared to results from the literature [6] in Fig. 3, and agreement to within 2% is obtained.

B. Coupled Microstrips on Dielectric Ridges

The geometry of two coupled microstrips on dielectric ridges is given in Fig. 4; the structure is characterized in Figs. 5–8. The first plot illustrates the behavior of the even- and odd-mode phase constants for different spacings over the frequency range 85–105 GHz. The next three plots show the phase constants β, characteristic impedances Z_c, and coupling coefficient k_c at 94 GHz as a function of spacing for strips on ridges and coupled microstrip on a continuous substrate.

Typical of coupled lines, the even-mode phase constants generally decrease and the odd-mode phase constants generally increase with increasing spacing (Figs. 5–6)—i.e., as the lines become further apart, the even and odd modes decouple and the phase constants tend toward the single-strip value. However, in this case, for $100\,\mu m < s < 150\,\mu m$, the odd-mode phase constant *decreases* before it begins to increase. At $s = 100\,\mu m$, the ridges are contiguous and the strips are together on a single ridge; the range $100\,\mu m < s < 150\,\mu m$ is a transition region between the case of two strips on a single ridge and the case of two strips on two ridges. The transition region is better understood by placing an electric wall halfway between the two strips; the odd mode may now be characterized by considering either the left or right half of the structure [28]. The capacitance between one of the strips and the electric wall through the dielectric
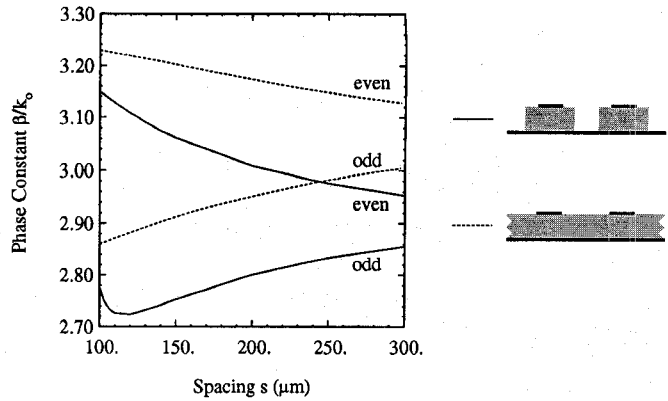

Fig. 6. Phase constant β versus spacing s at 94 GHz for microstrip on dielectric ridges (Fig. 4) and microstrip on continuous substrate (Fig. 4, with the two ridges replaced by a single substrate which extends over the entire width of the structure).
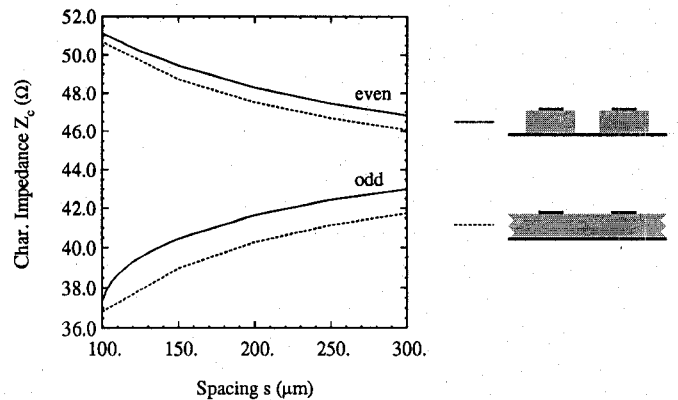

Fig. 7. Characteristic impedance Z_c versus spacing s at 94 GHz for microstrip on dielectric ridges (Fig. 4) and microstrip on continuous substrate (Fig. 4, with the two ridges replaced by a single substrate which extends over the entire width of the structure).
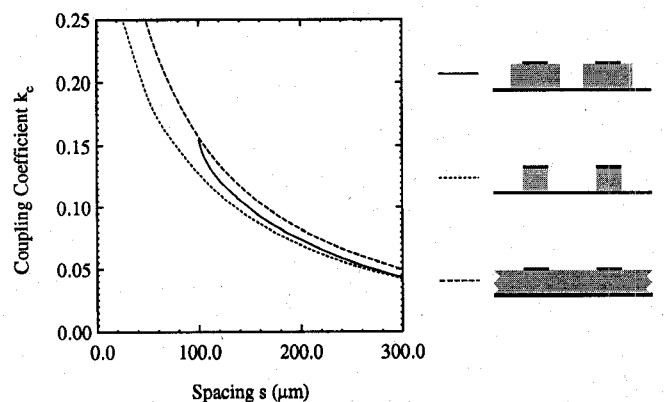

Fig. 8. Coupling coefficient k_c versus spacing s at 94 GHz for microstrip on dielectric ridges (Fig. 4), microstrip on narrower dielectric ridges (Fig. 4, with $d = 0$), and microstrip on continuous substrate (Fig. 4, with the two ridges replaced by a single substrate which extends over the entire width of the structure).

ridge and the air gap between the two ridges is sharply decreased when the air gap increases from zero width, and this decrease is reflected by the decrease of the odd-mode phase constant in the transition region. As the air gap increases, this
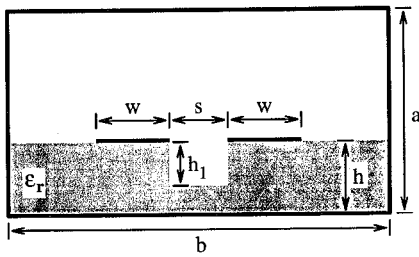
Fig. 9. Geometry of two microstrips with a groove etched between them: $w = 0.1$ mm, $h = 0.1$ mm, $s = 0.075$ mm, $a = 1.3$ mm, $b = 2.51$ mm, and $\epsilon_r = 12.85$.
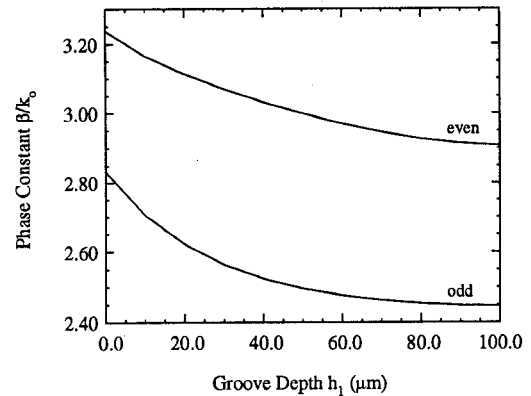

Fig. 10. Phase constant β versus groove depth h_1 at 94 GHz for coupled microstrip with etched groove (Fig. 9).
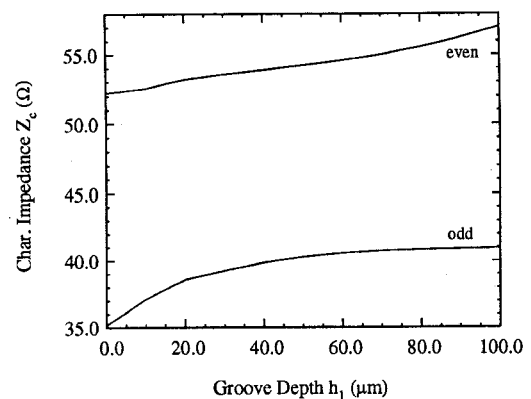

Fig. 11. Characteristic impedance Z_c versus groove depth h_1 at 94 GHz for coupled microstrip with etched groove (Fig. 9).
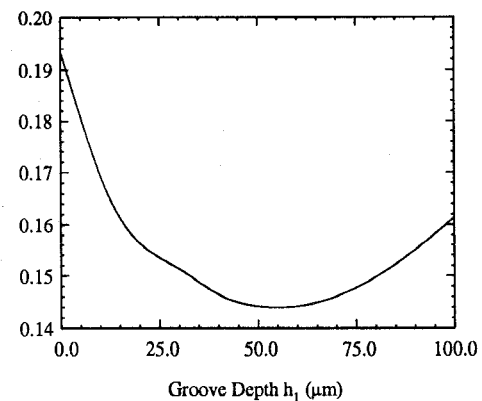

Fig. 12. Coupling coefficient k_c versus groove depth h_1 at 94 GHz for coupled microstrip with etched groove (Fig. 9).

capacitance becomes less and less significant compared to the other capacitances between the strip and ground, and the odd-mode β–s curve more closely resembles that of conventional coupled microstrip.

The data demonstrate that as the spacing between strips increases, the strips on the ridges decouple faster than the strips on the continuous substrate. The β–s and Z_c–s curves for the coupled microstrip on ridges converge to the respective values for a single strip on a ridge faster than the β–s and Z_c–s curves for the strips on the continuous substrate converge to the respective values for a single microstrip on a continuous substrate. In addition, the coupling coefficient of the strips on the ridges falls off more rapidly with spacing than does the coupling coefficient of microstrip on a continuous substrate. When increased packing density is desirable, structures of this type may be used in place of conventional microstrip.

The coupling coefficient curves include data for the limiting case of ridges with widths equal to the widths of the conducting strips. At $s = 100\,\mu$m, the strips on the wider ridges are on one ridge, and the coupling is the same as for microstrip on a continuous substrate. As s increases, the coupling of the strips on the wider ridges tends toward that of the strips on the narrower ridges. The transition between the case of strips on a contiguous substrate and strips on individual ridges over the range $100\,\mathrm{m} < s < 150\,\mu$m is again manifest.

C. Coupled Microstrips with an Etched Groove

A structure which is closely related to the microstrip on ridges is thecoupled microstrip with an etched groove (Fig. 9). The effects of groove depth on the propagation and coupling characteristics of the structure at 94 GHz are shown in Figs. 10–12.

The plots of the even- and odd-mode phase constants versus groove depth (Fig.10) show that the phase constants decrease rapidly with increasing groove depth at shallow groove depths, with the odd-mode phase constant decreasing more rapidly. As the groove depth becomes comparable to the substrate height, the decreases of the phase constants become slower and more alike. The odd-mode characteristic impedance also shows rapid change at shallow groove depths. Significant effects on the propagation occur when even a very shallow groove is added; the coupling coefficient versus groove depth plot in Fig. 12 shows that marked decoupling occurs over the range $0\,\mu$m $< h_1 < 20\,\mu$m.

Fig. 11 shows that the even- and odd-mode characteristic impedances are most dissimilar at very shallow and very deep groove depths, suggesting that the coupling coefficient has a minimum value at intermediate groove depths. Fig. 12 substantiates that k_c has such a minimum, and shows that the minimum occurs when the groove depth h_1 is between 50 and 60 μm.

Pulse propagation on the structure when $h_1 = 0\,\mu$m and $h_1 = 50\,\mu$m is illustrated in Figs. 13–15, respectively. In each case, the line lengths were 2.54 cm, and the lines were
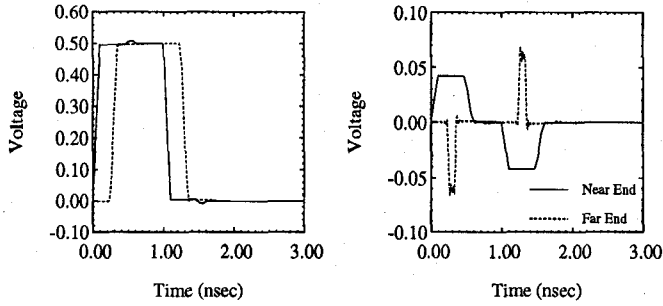
Fig. 13. Propagation of a pulse on coupled microstrip with no etched groove. The geometry is given in Fig. 9. Left—active line; right—sense line.
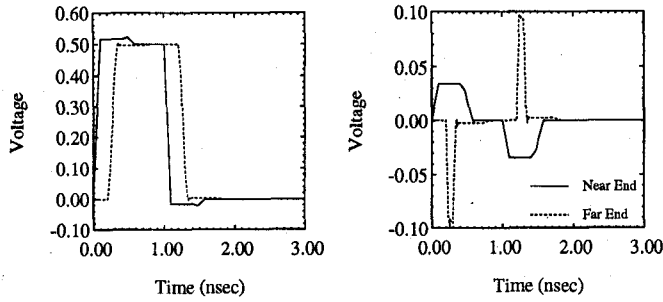

Fig. 14. Propagation of a pulse on coupled microstrip with an etched groove of depth $h_1 = 50\,\mu$m. The geometry is given in Fig. 9. Left—active line; right—sense line.

excited at one end of one of the lines, i.e., the "near end" of the "active line." The pulse had a duration of 1.0 ns, rise and fall times of 0.1 ns, an amplitude of 1.0 V, and a period of 10.0 ns. Each end was terminated with 43.0 Ω, which is the characteristic impedance of a single conducting strip on the substrate shown in Fig. 9 with $h_1 = 0\,\mu$m. Independent of groove depth, the pulse on the active line undergoes no noticeable dispersion since no losses are included, since the propagation constants are nearly constant at frequencies up to the maximum significant frequency component necessary for the construction of the pulse, and since the difference between the even- and odd-mode phase velocities is small.

The effects of the groove are quantified by the response on the "sense line" (i.e., the line without the source). Associated with the rise and fall of the pulse on the active line, relatively short, low-amplitude pulses are present at the near end of the sense line. Examination of these pulses shows that the presence of the groove lessens the crosstalk between the two lines at the near end. The amplitude of the near-end sense-line pulses in the ungrooved case is greater than the amplitude of the near-end sense-line pulses in the grooved case by a factor which is approximately equal to the ratio of the coupling coefficients when $h_1 = 0.0\,\mu$m and $h_1 = 50.0\,\mu$m. At the far end of the sense line, the dispersion due to the difference in even- and odd-mode phase velocities [29] causes the amplitude of the pulses to be larger in the grooved case.

The data demonstrate that the addition of the groove decreases crosstalk over short line lengths. The line length at which the groove ceases to improve the crosstalk may be determined from Fig. 15, which shows the time domain response at various points along the sense line. At line lengths
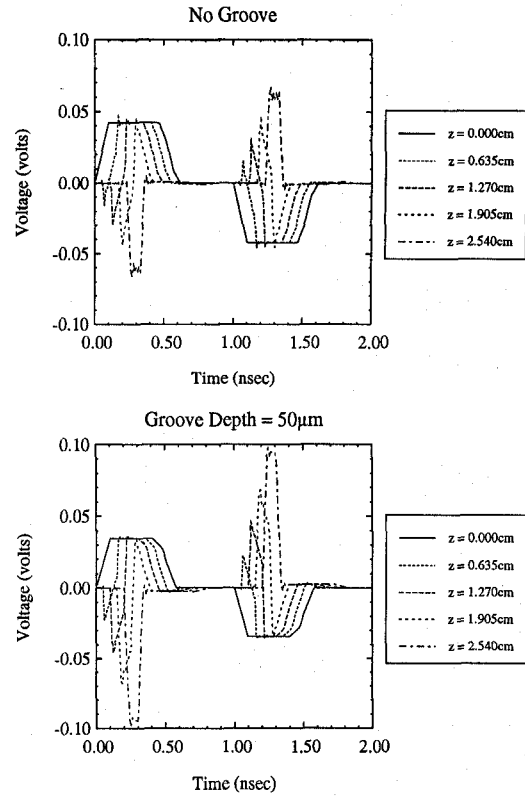

Fig. 15. Propagation of a pulse on the sense line of coupled microstrip with no etched groove (top) and with an etched groove of depth $h_1 = 50\,\mu$m (bottom). The geometry is given in Fig. 9.
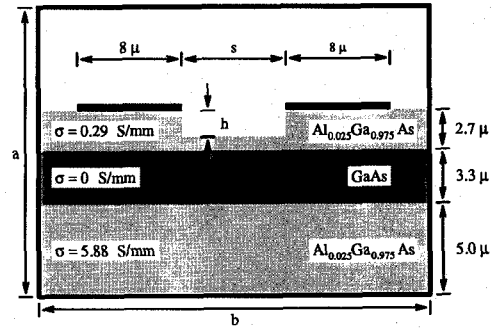

Fig. 16. Geometry of modulator structure. $a = b = 1.0$ mm.

of 0 and 0.635 cm, the maximum amplitude of the pulse in the grooved case is less than the maximum amplitude of the pulse in the ungrooved case; the converse is true at line lengths of 1.905 and 2.540 cm. At a line length of 1.270 cm, the maximum amplitude of the grooved case is only slightly greater than in the ungrooved case. The line length at which the groove begins to degrade performance is 1.25 cm.

D. Electrooptic Modulator Structures

The IEMM analysis technique may also be applied to electrooptic modulatorstructures. An integrated modulator structure (Fig. 16) typically consists of an intrinsic GaAs guiding layer for the optical signal and p– and n–$Al_{0.025}Ga_{0.975}As$ layers for top and bottom cladding. The modulator is fabricated on a 250 μm n$^+$–GaAs substrate; for simplicity, the substrate
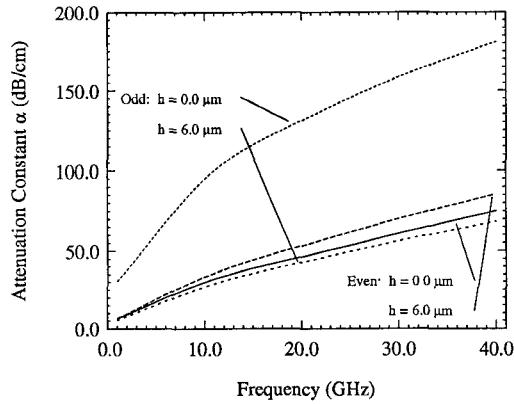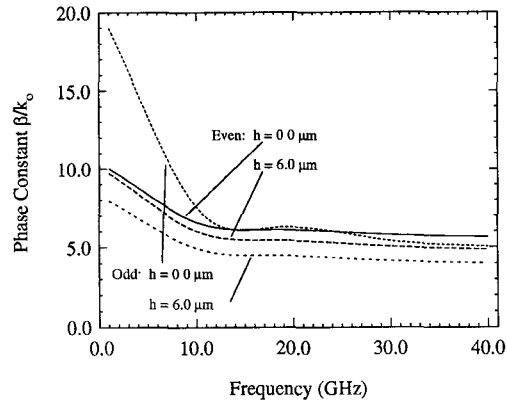
Fig. 17. Propagation constant $\gamma = \alpha + j\beta$ versus frequency for modulator structure of Fig. 16 at groove width $s = 8.0\,\mu$m and groove depths $h = 0.0\,\mu$m and $h = 6.0\,\mu$m.

Fig. 18. Propagation constant $\gamma = \alpha + j\beta$ versus groove width s for modulatorstructure of Fig. 16 at frequency = 18 GHz and groove depth $h = 6.0\,\mu$m.

has been assumed to be a perfect conductor in this case. The optical signal is modulated by a microwave signal, which is guided by the two conducting strips. The bandwidth depends inversely on the difference between the optical and microwave indexes of refraction [30]. The microwave index of refraction (i.e., β/k_0) is considerably larger than the optical index of refraction (= 3.41 for intrinsic GaAs at $\lambda = 1.3\,\mu$m [31]) due to the losses in the cladding layers. A groove is etched between the two electrodes in order to improve the bandwidth by decreasing the microwave index of refraction and to minimize the attenuation in the microwave signal.

The microwave phase and attenuation constants are plotted over the frequency range 1–40 GHz for two different groove depths in Fig. 17. As the frequency increases to 13 GHz, the phase constants β/k_0 decrease; at frequencies above 13 GHz, the phase constants are approximately constant at values between 4.0 and 6.0. The attenuation constants increase with frequency. The microwave frequency at which the difference between microwave and optical indexes of refraction is minimized, and at which microwave attenuation is minimized, is therefore approximately 13.0 GHz.

The behavior of the propagation constants as the groove width and height vary at 18 GHz is presented in Figs. 18–19. As the groove width s increases, the even and odd modes decouple as the phase constants converge; the attenuation is only slightly affected. As the groove depth h increases, the
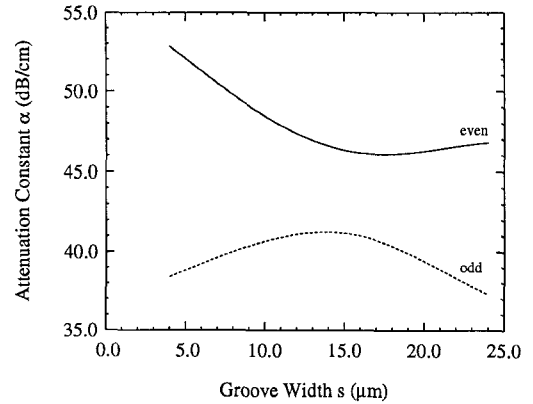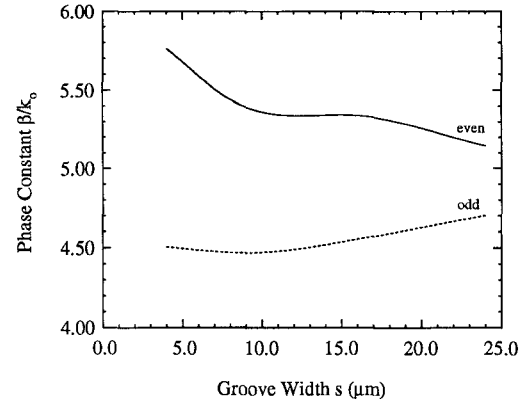
odd-mode attenuation decreases until the groove begins to penetrate the lossless layer, at which point the attenuation becomes approximately constant. This characteristic is consistent with the attenuation constant data over frequency, which show that the odd-mode attenuation constant when no groove is present ($h = 0.0\,\mu$m) is considerably higher than the other attenuation constants. The odd mode evidently has a large fraction of its power contained in the area between the conductors in the lossy cladding layer.

IV. CONCLUSION

An integral equation–mode matching method useful in the study of microstrip-ridge strutures has been presented, and the method was applied to the characterization of several nonplanar two-dimensional structures, namely, coupled microstrip on dielectric ridges, coupled microstrip with an etched groove, and an integrated electrooptic modulator. The IEMM technique is also applicable to structures with noncoplanar conductors, and like most other integral equation techniques, the IEMM technique is easily extended to the analysis of three-dimensional structures. Future studies could consider techniques to improve the efficiency of the method and modifications to the method which account for conductor losses, complex coplanar waveguide structures, and anisotropic materials.
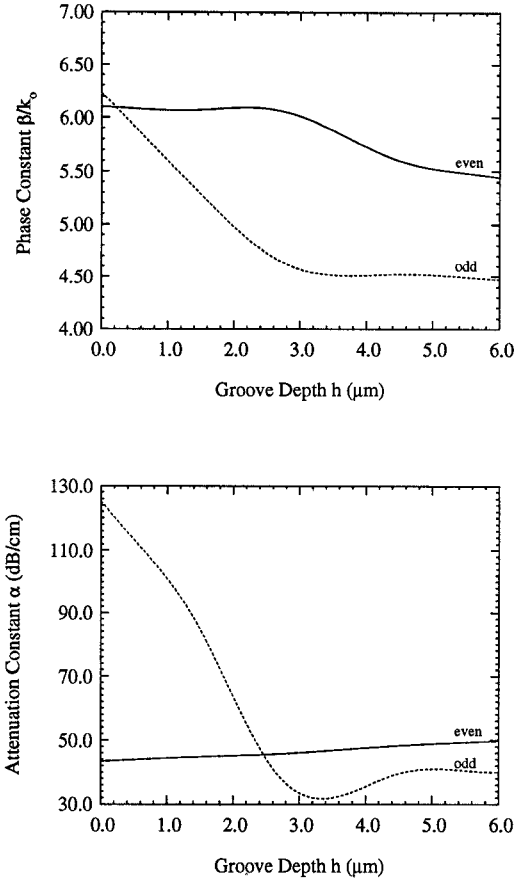
Fig. 19. Propagation constant $\gamma = \alpha + j\beta$ versus groove depth h for modulatorstructure of Fig. 16- at frequency = 18 GHz and groove width $s = 8.0\,\mu$m.

APPENDIX I

PRIMARY FIELD MODE AMPLITUDES

The y-dependencies of the primary fields are

$$
\left.
\begin{aligned}
&Y_{Pl}^{\lessgtr(j)E}(y, y') \\
&\quad = \pm C_{Pl}^{<(j)E} \exp\left(\pm j k_{yl}^{(j)E}(y - y')\right) \\
&Y_{Pl}^{\lessgtr(j)M}(y, y') \\
&\quad = C_{Pl}^{<(j)M} \exp\left(\pm j k_{yl}^{(j)M}(y - y')\right)
\end{aligned}
\right\} \quad y \lessgtr y'.
$$

(14)

The currents on the conducting strips are assumed to have only longitudinal (i.e., $\hat{z}$) components. Enforcing the boundary conditions at the source $(y = y')$ gives expressions for the primary field mode amplitudes:

$$
C_{Pl}^{<(j)E} = C_{Pl}^{>(j)E}
$$

$$
= \frac{j\omega X_l^{(ij)E}(x')}{2\epsilon^{(ij)}((k^{(ij)})^2 - (k_{xi}^{(ij)E})^2)I^E(l)}
$$

(15)

$$
C_{Pl}^{<(j)M} = C_{Pl}^{>(j)M}
$$

$$
= \frac{k_z}{k_{yl}^{(j)M}} \sum_{l'} C_{Pl'}^{<(j)E} I^{EM}(l', l)
$$

(16)

where

$$
I^{EM}(l, l') = \frac{1}{I^M(l')} \int_0^a \frac{1}{j\omega\epsilon^{(ij)}\epsilon^{(ij)}\mu^{(ij)}\mu^{(ij)}}
$$

$$
\cdot \frac{dX_l^{(ij)E}}{dx} X_{l'}^{(ij)M}(x)\, dx
$$

(17)

$$
I^E(l') = \int_0^a \frac{1}{\epsilon^{(ij)}\epsilon^{(i,j+1)}\mu^{(ij)}}
$$

$$
\cdot (X_{l'}^{(ij)E}(x))^2\, dx
$$

(18)

$$
I^M(l') = \int_0^a \frac{1}{\epsilon^{(ij)}\mu^{(ij)}\mu^{(i,j+1)}}
$$

$$
\cdot (X_{l'}^{(ij)M}(x))^2\, dx.
$$

(19)

APPENDIX II

EXPLICIT EXPRESSION FOR THE GREEN'S FUNCTION

Before presenting the explicit expression for the Green's function, the y-dependencies of the secondary fields are given, the interface scattering matrix is defined, and the secondary field mode amplitudes in the section which contains the source are determined.

The y-dependencies of the secondary fields are shown in (20) and (21) at the bottom of the next page.

The scattering matrices are defined by the equations

$$
\begin{bmatrix} L^{(j)}D^{(j)} \\ C^{(j+1)} \end{bmatrix}
$$

$$
= [S^{(j)}] \begin{bmatrix} L^{(j)-1}C^{(j)} \\ D^{(j+1)} + \Lambda^{(j+1)}(b^{(j)} - y')C_P^{<(j+1)} \end{bmatrix}
$$

$$
b^{(j)} < y'
$$

(22)

$$
\begin{bmatrix} L^{(j+1)}C^{(j+1)} \\ D^{(j)} \end{bmatrix}
$$

$$
= [S^{(j)}] \begin{bmatrix} L^{(j+1)-1}D^{(j+1)} \\ C^{(j)} + \Lambda^{(j)}(y' - b^{(j)})C_P^{>(j)} \end{bmatrix}
$$

$$
b^{(j)} > y'
$$

(23)

where $C^{(j)}, D^{(j)}, C^{(j+1)}, D^{(j+1)}, C_P^{<(j+1)}$, and $C_P^{>(j)}$ are vectors which contain the mode amplitudes, $L^{(j)\pm 1}$ is given in (8) and

$$
\Lambda^{(j)}(d) = \text{diag}\{\exp\left(j k_{yl}^{(j)} d\right)\}.
$$

(24)

The general form of the mode amplitude vectors is

$$
C^{(j)} = [C_1^{(j)M}\, C_2^{(j)M} \cdots C_l^{(j)M} \cdots C_1^{(j)E}
$$

$$
\cdot C_2^{(j)E} \cdots C_l^{(j)E} \cdots]^T.
$$

(25)

The primary fields are included in the boundary conditions via the vectors C_P (Appendix I); recall that $C_P^{(j)} = 0$ unless section j contains the source.

If section j is now assumed to contain the source, then section j is divided into two regions at $y = y'$, and $C_l^{<(j)}$ and $D_l^{<(j)}$ are the mode amplitudes for $y < y'$ and $C_l^{>(j)}$ and $D_l^{>(j)}$ are the mode amplitudes for $y > y'$. The reflection coefficient matrix definitions ((6) and (9)) with nonzero primary fields are

$$
C^{<(j)}
$$

$$
= \Gamma^{<(j)}(D^{<(j)} + \Lambda^{(j)}(b^{(j-1)} - y')C_P^{<(j)})
$$

(26)

$$
D^{>(j)}
$$

$$
= \Gamma^{>(j)}(C^{>(j)} + \Lambda^{(j)}(y' - b^{(j)})C_P^{>(j)})
$$

(27)

and $C^{>(j)}$ and $D^{<(j)}$ are

$$
\begin{aligned}
C^{>(j)} &= (I - L^{(j)-1}\Gamma^{<(j)}L^{(j)-1}\Gamma^{>(j)})^{-1} \\
&\quad \cdot L^{(j)-1}\Gamma^{<(j)} \\
&\quad \cdot (L^{(j)-1}\Gamma^{>(j)}\Lambda^{(j)}(y' - b^{(j)})C_P^{>(j)} \\
&\quad + \Lambda^{(j)}(b^{(j-1)} - y')C_P^{<(j)}) \\
&\equiv R_1^{>(j)}\Lambda^{(j)}(y' - b^{(j)})C_P^{>(j)} + R_2^{>(j)} \\
&\quad \cdot \Lambda^{(j)}(b^{(j-1)} - y')C_P^{<(j)} \qquad (28)
\end{aligned}
$$

$$
\begin{aligned}
D^{<(j)} &= (I - L^{(j)-1}\Gamma^{>(j)}L^{(j)-1}\Gamma^{<(j)})^{-1} \\
&\quad \cdot L^{(j)-1}\Gamma^{>(j)} \\
&\quad \cdot (L^{(j)-1}\Gamma^{<(j)}\Lambda^{(j)}(b^{(j-1)} - y')C_P^{<(j)} \\
&\quad + \Lambda^{(j)}(y' - b^{(j)})C_P^{>(j)}) \\
&\equiv R_1^{<(j)}\Lambda^{(j)}(b^{(j-1)} - y')C_P^{<(j)} \\
&\quad + R_2^{<(j)}\Lambda^{(j)}(y' - b^{(j)})C_P^{>(j)}. \qquad (29)
\end{aligned}
$$

The secondary field mode amplitudes are determined from (28) and (27) if the Green's function is required for $y < y'$, or from (29) and (26) if the Green's function is required for $y > y'$. Typically, the conductors are at section interfaces, so that either $y' = b^{(j)}$ or $y' = b^{(j-1)}$. Inspection of the above equations indicates that numerical problems are minimized when the Green's function for $y < y'$ is used in the case when $y' = b^{(j-1)}$ and the Green's function for $y > y'$ is used in the case when $y' = b^{(j)}$.

As shown in (11), the Green's function is determined by the vectors $U_1^{(j)}(x,y)$ and $U_2^{(j)}(x',y')$ and by the matrix $R^{(j)}$.

The vector $U_1^{(j)}(x,y)$ is

$$
\begin{aligned}
&U_1^{(j)}(x,y) \\
&= \begin{bmatrix} \Lambda^{(j)}(d^{\leq(j)}(y)) & U^{(j)}(x) \\ \Lambda^{(j)}(d^{\geq(j)}(y)) & U^{(j)}(x) \\ \Lambda^{(j)}(d^{\leq(j)}(y)) & U^{(j)}(x) \\ \Lambda^{(j)}(d^{\geq(j)}(y)) & U^{(j)}(x) \end{bmatrix} \quad y \lessgtr y' \quad (30)
\end{aligned}
$$

where the lth element of the vector $U^{(j)}(x)$ is

$$
U_l^{(j)}(x) = \begin{cases} -\dfrac{k_z}{\omega\epsilon^{(ij)}\mu^{(ij)}}\dfrac{dX_l^{(ij)M}}{dx} \\ \qquad \text{if } l \text{ denotes a TM}_x \text{ mode} \\ -\dfrac{jk_{yl}^{(j)E}}{\epsilon^{(ij)}}X_l^{(ij)E}(x) \\ \qquad \text{if } l \text{ denotes a TE}_x \text{ mode} \end{cases} \quad (31)
$$

and $d^{<(j)}(y) = b^{(j-1)} - y$ and $d^{>(j)}(y) = y - b^{(j)}$. The vector $U_2^{(j)}(x',y')$ is

$$
\begin{aligned}
&U_2^{(j)}(x',y') \\
&= \begin{bmatrix} \Lambda^{(j)}(d^{\leq(j)}(y)) & C_P^{<(j)}(x') \\ \Lambda^{(j)}(d^{\geq(j)}(y)) & C_P^{<(j)}(x') \\ \Lambda^{(j)}(d^{\leq(j)}(y)) & C_P^{<(j)}(x') \\ \Lambda^{(j)}(d^{\geq(j)}(y)) & C_P^{(j)}(x') \end{bmatrix} \quad y \lessgtr y'. \quad (32)
\end{aligned}
$$

Finally, the matrix $R^{(j)}$ is shown in (33) at the bottom of the page.

$$
Y_l^{(j)E}(y) = \begin{cases} \left.\begin{array}{l} C_l^{(j)E}\exp\left(-jk_{yl}^{(j)E}(y - b^{(j-1)})\right) \\ \quad + D_l^{(j)E}\exp\left(jk_{yl}^{(j)E}(y - b^{(j-1)})\right) \end{array}\right\} & y < y' \\ \left.\begin{array}{l} -C_l^{(j)E}\exp\left(-jk_{yl}^{(j)E}(y - b^{(j)})\right) \\ \quad + D_l^{(j)E}\exp\left(jk_{yl}^{(j)E}(y - b^{(j)})\right) \end{array}\right\} & y > y' \end{cases}
$$

$$(20)$$

$$
Y_l^{(j)M}(y) = \begin{cases} \left.\begin{array}{l} C_l^{(j)M}\exp\left(-jk_{yl}^{(j)M}(y - b^{(j-1)})\right) \\ \quad + D_l^{(j)M}\exp\left(jk_{yl}^{(j)M}(y - b^{(j-1)})\right) \end{array}\right\} & y < y' \\ \left.\begin{array}{l} -C_l^{(j)M}\exp\left(-jk_{yl}^{(j)M}(y - b^{(j)})\right) \\ \quad + D_l^{(j)M}\exp\left(jk_{yl}^{(j)M}(y - b^{(j)})\right) \end{array}\right\} & y > y'. \end{cases}
$$

$$(21)$$

$$
R^{(j)} = \begin{bmatrix} I + R_1^{\lessgtr(j)} & 0 & 0 & 0 \\ 0 & R_2^{\lessgtr(j)} & 0 & 0 \\ 0 & 0 & \Gamma^{\lessgtr(j)}(I + R_1^{\lessgtr(j)}) & 0 \\ 0 & 0 & 0 & \Gamma^{\lessgtr(j)}R_2^{\lessgtr(j)} \end{bmatrix} \quad y \lessgtr y'. \quad (33)
$$

APPENDIX III

COUPLING COEFFICIENT

The coupling coefficient k_c is given by

$$k_c = \tfrac{1}{2}(\Gamma_e - \Gamma_o) \tag{34}$$

where

$$\Gamma_e = \frac{j(\overline{Z}_{ce} - \overline{Z}_{ce}^{-1}) \sin \beta_e l}{2 \cos \beta_e l + j(\overline{Z}_{ce} + \overline{Z}_{ce}^{-1}) \sin \beta_e l} \tag{35}$$

$$\Gamma_o = \frac{j(\overline{Z}_{co} - \overline{Z}_{co}^{-1}) \sin \beta_o l}{2 \cos \beta_o l + j(\overline{Z}_{co} + \overline{Z}_{co}^{-1}) \sin \beta_o l} \tag{36}$$

$$\overline{Z}_{ce} = \frac{Z_{ce}}{Z_o} \tag{37}$$

$$\overline{Z}_{co} = \frac{Z_{co}}{Z_o} \tag{38}$$

$$Z_o = \sqrt{Z_{ce} Z_{co}} \tag{39}$$

where Z_{ce} and Z_{co} are the characteristic impedances; β_e and β_o are the phase constants for the even and odd modes, respectively; and the length l of the coupler is taken to be one-quarter of the average of the even- and odd-mode wavelengths.

REFERENCES

[1] A. G. Engel, Jr. and P. B. Katehi, "Low-loss monolithic transmission lines for submillimeter and terahertz frequency applications," *IEEE Trans. Microwave Theory Tech.*, vol. 39, pp. 1847–1854, Nov. 1991.

[2] B. Young and T. Itoh, "Analysis and design of microslab waveguide," *IEEE Trans. Microwave Theory Tech.*, vol. MTT-35, pp. 850–857, Sept. 1987.

[3] ——, "Analysis of coupled Microslab™ lines," *IEEE Trans. Microwave Theory Tech.*, vol. 36, pp. 616–619, Mar. 1988.

[4] C. E. Smith and R. Chang, "Microstrip transmission line with finite-width dielectric," *IEEE Trans. Microwave Theory Tech.*, vol. MTT-28, pp. 90–94, Feb. 1980.

[5] E. Yamashita, K. R. Li, and Y. Suzuki, "Characterization method and simple design formulas of MCS lines proposed for MMIC's," *IEEE Trans. Microwave Theory Tech.*, vol. MTT-35, pp. 1355–1362, Dec. 1987.

[6] E. Yamashita, H. Ohashi, and K. Atsuki, "Characterization of microstrip lines near a substrate edge and design formulas of edge-compensated microstrip lines," *IEEE Trans. Microwave Theory Tech.*, vol. 37, pp. 890–896, May 1989.

[7] W. Heinrich and H. L. Hartnagel, "Wave propagation on MESFET electrodes and its influence on transistor gain," *IEEE Trans. Microwave Theory Tech.*, vol. MTT-35, pp. 1–8, Jan. 1987.

[8] C. C. Tzuang and J.-D. Tseng, "A full-wave mixed potential mode-matching method for the analysis of planar or quasi-planar transmission lines," *IEEE Trans. Microwave Theory Tech.*, vol. 39, pp. 1701–1711, Oct. 1991.

[9] M. Thorburn, A. Agoston, and V. K. Tripathi, "Computation of frequency-dependent propagation characteristics of microstriplike propagation structures with discontinuous layers," *IEEE Trans. Microwave Theory Tech.*, vol. 38, pp. 148–153, Feb. 1990.

[10] K. Wu and R. Vahldieck, "Comprehensive MoL analysis of a class of semiconductor-based transmission lines suitable for microwave and optoelectronic application," *Int. J. Numer. Modelling: Electron. Networks, Devices and Fields*, vol. 4, pp. 45–62, 1991.

[11] B. M. A. Rahman, F. A. Fernandez, and J. B. Davies, "Review of finite element methods for microwave and optical waveguides," *Proc. IEEE*, vol. 79, pp. 1442–1448, Oct. 1991.

[12] K. Bierwirth, N. Schulz, and F. Arndt, "Finite-difference analysis of rectangular dielectric waveguide structures," *IEEE Trans. Microwave Theory Tech.*, vol. MTT-34, pp. 1104–1114, Nov. 1986.

[13] D. H. Choi and W. J. R. Hoefer, "The finite-difference-time-domain method and its application to eigenvalue problems," *IEEE Trans. Microwave Theory Tech.*, vol. MTT-34, pp. 1464–1470, Dec. 1986.

[14] W. J. R. Hoefer, "The transmission-line matrix method—Theory and applications," *IEEE Trans. Microwave Theory Tech.*, vol. MTT-33, pp. 882–893, Oct. 1985.

[15] W. Schroeder and I. Wolff, "A new hybrid mode boundary integral method for analysis of MMIC waveguides with complicated crossection," in *1989 IEEE MTT-S Int. Microwave Symp. Dig.*, vol. 2, 1989, pp. 711–714.

[16] A. G. Engel, Jr. and L. P. B. Katehi, "On the analysis of a transition to a layered ridged dielectric waveguide," in *1992 IEEE MTT-S Int. Microwave Symp. Dig.*, vol. 2, 1992, pp. 983–986.

[17] ——, "Analysis of microstrip structures on and near dielectric ridges using an integral equation-mode matching technique," in *1991 IEEE MTT-S Int. Microwave Symp. Dig.*, vol. 1, 1991, pp. 135–138.

[18] F. E. Gardiol, "Higher-order modes in dielectrically loaded rectangular waveguides," *IEEE Trans. Microwave Theory Tech.*, vol. MTT-16, pp. 919–924, Nov. 1968.

[19] R. Safavi-Naini and R. H. MacPhie, "On solving waveguide junction scattering problems by the conservation of complex power technique," *IEEE Trans. Microwave Theory Tech.*, vol. MTT-29, pp. 337–343, Apr. 1981.

[20] ——, "Scattering at rectangular-to-rectangular waveguide junctions," *IEEE Trans. Microwave Theory Tech.*, vol. MTT-30, pp. 2060–2063, Nov. 1982.

[21] R. R. Mansour and R. H. MacPhie, "Scattering at an N-furcated parallel-plate waveguide-junction," *IEEE Trans. Microwave Theory Tech.*, vol. MTT-33, pp. 337–343, Sept. 1985.

[22] ——, "An improved transmission matrix formulation of cascaded discontinuities and its application to E-plane circuits," *IEEE Trans. Microwave Theory Tech.*, vol. MTT-34, pp. 1490–1498, Dec. 1986.

[23] J. Meixner, "The behavior of electromagnetic fields at edges," *IEEE Trans. Antennas Propagat.*, vol. AP-20, pp. 442–446, July 1972.

[24] L. Wiemer and R. H. Jansen, "Reciprocity related definition of strip characteristic impedance for multiconductor hybrid-mode transmission lines," *Microwave Opt. Tech. Lett.*, vol. 1, pp. 22–25, Mar. 1988.

[25] L. Carin and K. J. Webb, "Characteristic impedance of multilevel, multiconductor hybrid mode microstrip," *IEEE Trans. Magn.*, vol. 25, pp. 2947–2949, July 1988.

[26] P. A. Rizzi, *Microwave Engineering.* Englewood Cliffs, NJ: Prentice-Hall, 1988, p. 383.

[27] L. Carin and K. J. Webb, "An equivalent circuit model for terminated hybrid-mode multiconductor transmission lines," *IEEE Trans. Microwave Theory Tech.*, vol. 37, pp. 1784–1793, Nov. 1989.

[28] K. C. Gupta, R. Garg, and I. J. Bahl, *Microstrip Lines and Slotlines.* Dedham, MA: Artech House, 1979, ch. 8.

[29] J. P. Gilb and C. A. Balanis, "Pulse distortion on multilayer coupled microstrip lines," *IEEE Trans. Microwave Theory Tech.*, vol. 37, pp. 1620–1628, Oct. 1989.

[30] R. C. Alferness, S. K. Korotky, and A. J. Marcatili, "Velocity-matching techniques for integrated optic traveling wave switch/modulators," *IEEE J. Quantum Electron.*, vol. QE-20, pp. 301–309, Mar. 1984.

[31] S. Y. Wang and S. H. Lin, "High speed III–V electrooptic waveguide modulators at $\lambda = 1.3 \ \mu m$," *J. Lightwave Technol.*, vol. 6, pp. 758–771, June 1988.

Andrew G. Engel, Jr. was born in Rochester, MN, on February 9, 1961. He received the B.S. degree in physics from Stanford University, Stanford, CA, in 1982, and the M.S. and Ph.D. degrees in electrical engineering from the University of Michigan, Ann Arbor, in 1988 and 1993, respectively.

From 1984 to 1987 he worked at Avantek, Inc., Santa Clara, CA, as a Microwave Components Reliability Engineer. His Ph.D. dissertation at the University of Michigan was on the frequency and time domain characterization of microwave, millimeter-wave, and terahertz hybrid and monolithic waveguiding structures. He is currently with Motorola, Phoenix, AZ.

Linda P. B. Katehi (S'81–M'84–SM '89) received the B.S.E.E. degree from the National Technical University of Athens, Greece, in 1977, and the M.S.E.E. and Ph.D. degrees from the University of California, Los Angeles, in 1981 and 1984, respectively.

In September 1984 she joined the faculty of the EECS Department of the University of Michigan, Ann Arbor. Since then, she has been involved in the modeling and computer-aided design of millimeter and near-millimeter wave monolithic circuits and antennas.

ptIn 1984 Dr Katehi received teh W. P. King Award and in 1985 the S. A. Schelkunoff Award from the Antennas and Propagation Society. In 1987 she received an NSF Presidential Young Investigator Award and an URSI Young Scientist Fellowship. She is an Associate Editor of the IEEE Antennas and Propagation Society and Radio Science. She is also a member of Sigma Xi, URSI Commission D, and an elected member of the IEEE Antennas and Propagation Society Administrative Committee.